

Metastable phase equilibria in the ice II stability field. A Raman study of synthetic high-density water inclusions in quartz

Yves Krüger, Lionel Mercury, Aurélien Canizares, Dominik Marti, Patrick Simon

▶ **To cite this version:**

Yves Krüger, Lionel Mercury, Aurélien Canizares, Dominik Marti, Patrick Simon. Metastable phase equilibria in the ice II stability field. A Raman study of synthetic high-density water inclusions in quartz. Physical Chemistry Chemical Physics, 2019, 21, pp.19554-19566. 10.1039/c9cp03647d . insu-02274539

HAL Id: insu-02274539
https://insu.hal.science/insu-02274539

Submitted on 3 Sep 2019

HAL is a multi-disciplinary open access archive for the deposit and dissemination of scientific research documents, whether they are published or not. The documents may come from teaching and research institutions in France or abroad, or from public or private research centers.

L'archive ouverte pluridisciplinaire **HAL**, est destinée au dépôt et à la diffusion de documents scientifiques de niveau recherche, publiés ou non, émanant des établissements d'enseignement et de recherche français ou étrangers, des laboratoires publics ou privés.



Distributed under a Creative Commons Attribution - NonCommercial - NoDerivatives 4.0 International License



PCCP

Metastable phase equilibria in the ice II stability field. A Raman study of synthetic high-density water inclusions in quartz

Journal:	*Physical Chemistry Chemical Physics*
Manuscript ID	CP-ART-06-2019-003647
Article Type:	Paper
Date Submitted by the Author:	28-Jun-2019

Complete List of Authors:	Krüger, Yves; University of Bergen Faculty of Mathematics and Natural Sciences, Department of Earth Science Mercury, Lionel; Institut des Sciences de la Terre, Canizares, Aurélien; CEMHTI-CNRS UPR 3079 Marti, Dominik; Technical University of Denmark, Department of Health Technology Simon, Patrick; CNRS, CEMHTI-CNRS UPR3079

SCHOLARONE™
Manuscripts

Article type: Full paper

Website www.rsc.org/pccp
Impact factor* 3.906

Journal expectations To be suitable for publication in *Physical Chemistry Chemical Physics* (*PCCP*) articles must include significant new innovation and/or insight into physical chemistry.

Article type: Full paper Original scientific work that has not been published previously. Full papers do not have a page limit and should be appropriate in length for scientific content.

Authors should include a brief discussion in the Introduction that sets the context for the new work and gives their motivation for carrying out the study.

Journal scope Visit the *PCCP* website for additional details of the journal scope and expectations.

The journal has a broad scope which includes spectroscopy, dynamics, kinetics, statistical mechanics, thermodynamics, electrochemistry, catalysis, surface science, quantum mechanics and theoretical developments. Interdisciplinary research areas such as polymers and soft matter, materials, nanoscience, energy, surfaces/interfaces, and biophysical chemistry are welcomed if they demonstrate significant new innovation and/or insight into physical chemistry.

Reviewer responsibilities Visit the Reviewer responsibilities website for additional details of the reviewing policy and procedure for Royal of Society of Chemistry journals.

When preparing your report, please:

- Focus on the originality, importance, impact and reliability of the science. English language and grammatical errors do not need to be discussed in detail, except where it impedes scientific understanding.
- Use the journal scope and expectations to assess the manuscript's suitability for publication in *PCCP.*
- State clearly whether you think the article should be accepted or rejected and include details of how the science presented in the article corresponds to publication criteria.
- Inform the Editor if there is a conflict of interest, a significant part of the work you cannot review with confidence or if parts of the work have previously been published.

Thank you for evaluating this manuscript, your advice as a reviewer for *PCCP* is greatly appreciated.

Dr Anna Simpson Executive Editor
Royal Society of Chemistry, UK

Professor David Rueda Editorial Board Chair
Imperial College London, UK

**2017 Journal Citation Reports (Clarivate Analytics, 2018)*

Dear Editor

We would like to submit our manuscript "*Metastable phase equilibria in the ice II stability field. A Raman study of synthetic high-density water inclusions in quartz*" for publication in PCCP. This experimental work reports on three metastable phase equilibria within the ice II stability field: ice I_h + liquid, ice I_h + ice IV, and I_h + ice III. It is the first time that high-pressure ices have been identified in fluid inclusions and to our knowledge, this is the first study reporting on the existence of a metastable ice I_h-ice IV equilibrium line terminating in a metastable ice I_h-ice IV-liquid triple point at the intersection with the low-temperature metastable extension of the I_h melting curve at -32.7 °C and 273 MPa. In fluid inclusions the pressures cannot be measured directly but in the present study we were able to calculate equilibrium pressures based on the peak positions of the ice I_h Raman bands. To do so the paper additionally presents a new calibration of the temperature- and pressure-dependent shift of the ice I_h Raman bands ($(\partial \nu/\partial T)_{p = \text{const}}$ and $(\partial \nu/\partial p)_{T = \text{const.}}$).

Our manuscript presents a wealth of new experimental data and in the discussion part we correlate them with available literature data in order to draw a consistent picture of the phase relations in this specific region of the water phase diagram.

We believe that PCCP would be an appropriate journal to publish this study. We thank you for considering our manuscript and look forward to receiving constructive comments and criticisms from the reviewers.

Sincerely,

Yves Krüger

Received 00th January 20xx,
Accepted 00th January 20xx

DOI: 10.1039/x0xx00000x

Metastable phase equilibria in the ice II stability field. A Raman study of synthetic high-density water inclusions in quartz

Yves Krüger[a,d*], Lionel Mercury[a], Aurélien Canizarès[b], Dominik Marti[c], and Patrick Simon[b]

Microthermometric measurements of a synthetic high-density (984 kg/m^3) pure water inclusion in quartz revealed that only part of the super-cooled liquid water (L) transforms to solid ice I_h upon ice nucleation (L → ice I_h + L). While ice nucleation occurs in the ice I_h stability field at –41 °C and 28 MPa the pressure increases instantaneously to 315 MPa into the ice II stability field, where both phases, liquid water and ice I_h are metastable. The coexistence of these two phases was confirmed by Raman spectroscopy and could be traced down to –80 °C. The pressure along this low-temperature metastable extension of the ice I_h melting curve was determined by means of the frequency shift of the ice I_h peak position using both the O–H stretching band around 3100 cm^{-1} and the lattice translational band around 220 cm^{-1}. At –80 °C and 466 MPa the supercooled ice I_h melting curve encounters the homogeneous nucleation limit (T_H) and the remaining liquid water transformed either to metastable ice IV (ice I_h + L→ ice I_h + ice IV) or occasionally to metastable ice III (ice I_h + L→ ice I_h + ice III). The nucleation of ice IV resulted in a pressure drop of about 180 MPa. Upon subsequent heating the pressure develops along a slightly negatively sloped ice I_h-ice IV equilibrium line terminating in a triple point at –32.7 °C and 273 MPa, where ice IV melts to liquid water (ice I_h + ice IV → ice I_h + L). To our knowledge, the existence of both the metastable I_h-ice IV binodal and the corresponding triple point has not yet been reported in the literature. Hitherto existing experimental data of the ice IV melting curve, finally, were found to be in line with the observed ice I_h-ice IV-liquid triple point.
If, on the other hand, ice III nucleated at –80 °C (instead of ice IV) the associated pressure drop was about 260 MPa. The ice I_h-ice III-liquid triple point, was determined at –22.0 °C and 207 MPa (ice I_h + ice III → ice I_h + L), which is in agreement with previous experimental data.

Introduction

The phase diagram of water ices is a fascinating topic of research because of the multitude of ice polymorphs with a corresponding multitude of equilibrium curves and triple points (*cf.* reviews [1, 2], and references therein). About 18 crystalline ice polymorphs (ice I (h and c) – ice XVII) and three amorphous ice phases (LDA, HDA, VHDA) have been identified so far. Owing to the large number of ice polymorphs and extensive metastability of these phases outside their range of stability (e.g. Bridgman [3], p. 530-533), the phase diagram of solid water is fairly complex. Moreover, two of the ice polymorphs, ice IV and ice XII, exist only in metastable form within the stability fields of other ice phases. The crystalline ices are subdivided in two structural groups, in those featuring proton-disordered structures (ices I_h, III, IV, V, VI, VII and XII), and those with proton-ordered structures e.g. ices II, VIII, IX, XI. Ices with proton-disordered structures have all in common that they share a stable or metastable (ices IV and XII) phase boundary with liquid water. Extensions of these ice melting curves beyond their stability

[a.] *Institut des Sciences de la Terre d'Orléans (ISTO), UMR7327 Université d'Orléans, CNRS-INSU, Bureau de Recherches Géologiques et Minières (BRGM), 45071 Orléans, France Address here.*
[b.] *CEMHTI-CNRS UPR3079, 45071 Orléans, France*
[c.] *Department of Health Technology, DTU, 4000 Roskilde, Denmark*
[d.] *Present address: Department of Earth Science, University of Bergen, 5007 Bergen, Norway*
* Corresponding author: yves.kruger@uib.no

ranges into metastable domains are common and have been reported for several ice phases.[4-8] Furthermore, it is also known that, liquid water can be super-cooled below its freezing temperature by up to 70 °C,[9] and the ice phase that eventually forms upon freezing is always proton-disordered.

Experimental investigations of the ice phase diagram are typically performed in pressure cells in order to produce the high-pressure ice phases to be investigated (e.g. refs. [3,4,8-10]). The occurrence of phase transitions (crystallisation or melting) induced by pressure and temperature changes are recorded by means of differential thermal analyses and/or by volume changes of the ice/water sample. The technique is relatively simple and allows full control on temperature, pressure and volume. Fluid inclusions, in contrast, are closed microscopic systems in a crystal, in which the pressure changes as a function of temperature and density (isochores), and hence, is not an independent variable of the experiment. The optical transparency of the host crystal, however, allows for direct visual observations of the phase transitions and an in-situ identification of the phases by Raman spectroscopy. In previous experimental studies synthetic fluid inclusions have successfully been used to explore the metastable super-heated domain of liquid water reaching negative pressures of up to –140 MPa.[11-15] The present study uses this experimental approach to explore metastable phase equilibria at temperatures below ice nucleation. Recently, an extensive experimental study has been published by Qiu et al.[15] exploring the low-temperature metastable region of liquid water using synthetic fluid inclusions in quartz. By means of classical fluid inclusion microthermometry they measured temperatures (T) of a series of different phase transitions as a function of density (ϱ) in the temperature range between 150 and –43 °C determining the ϱ-T trends of 1. the ice nucleation curve at negative pressures, 2. the ice I_h melting curve at negative pressures, 3. the super-cooled saturation curve, and 4. the line of spontaneous vapour bubble nucleation (cavitation) at high negative pressures. The present study ties in with the work of Qiu et al. by extending it to temperatures below ice nucleation. The nucleation of ordinary ice I_h in (nearly) isochoric systems like fluid inclusions forcibly results in an intense increase of pressure due to the larger volume of ice compared to liquid water. For high-density inclusions it is thus expected that the pressure increases well above 200 MPa upon ice nucleation, transferring the system into the ice II stability field (*cf.* ref. [3]). In consideration of such high pressures it was somehow surprising to see that irreversible volume changes of the inclusions due to brittle and/or plastic deformation were very small, indicated by only slight increases of subsequently re-measured liquid–vapour homogenisation temperatures (T_h). Furthermore, it was observed that irreversible volume changes did not systematically increase with increasing water densities of the inclusions. The initial motivation for conducting this study, therefore, was to identify the ice phase(s) actually present in the inclusions after nucleation using Raman spectroscopy. In contrast to Qiu et al. who assumed that liquid water transforms completely to solid upon ice nucleation, attentive microthermometric observations revealed that a small fraction of liquid water remains in the inclusion coexisting with ice. This finding has opened a new pathway to investigate both solid-liquid and solid-solid phase relations in the water phase diagram by means of synthetic fluid inclusions.

The Material and Methods section describes the synthetic fluid inclusion samples used for this study, the experimental setup, and the Raman measurements. We then report on the results of the microthermometric and Raman spectroscopic measurements, on a new calibration to quantify the shift of the ice I_h Raman bands as a function of temperature and pressure, and we present a p-T phase diagram. The results will then be discussed and compared to available literature data.

Materials and Methods

Fluid inclusion samples

For the present study we used new thick-sections cut from the same synthetic fluid inclusion samples that had been used by Qiu et al.[15] The synthetic fluid inclusions were produced in sealed gold capsules containing only deionised (air-saturated) water and pre-fractured inclusion-free natural quartz that was cut to prisms perpendicular to the quartz c-axis. No additives like silica gel or NaOH were used to enhance quartz solubility during hydrothermal synthesis and no excess air was trapped in the sealed capsules. Hydrothermal syntheses were performed in an internally heated pressure vessel in the HP-GeoMatS Laboratory at GFZ Potsdam. For our study we selected a high-density (984 kg/m^3) fluid inclusion with a size of approximately 120 µm^3 (inclusion A, sample MW15). Synthesis conditions of sample MW15 were at 460 °C and 860 MPa for a run duration of 54 hours. After hydrothermal synthesis, the quartz prism, now containing numerous fluid inclusions along the healed fractures, was cut to sections of approximately 300 µm thickness with the cutting faces approximately parallel to the quartz c-axis. The sections were then polished on both sides to make them transparent for microscopic observation of the fluid inclusions in transmitted light. For a detailed description of the synthesis procedure and sample preparation we refer to Qiu et al.[15] (*Supplementary Material*).

Inclusion A selected for this study is in a metastable liquid state at room temperature. Single ultra-short laser pulses were used to stimulate vapour bubble nucleation[16], thus transferring the inclusion from a metastable liquid to a stable liquid-vapour two-phase state. Subsequently, the density of the encapsulated water and the volume of the inclusion were determined based on of the measured liquid–vapour homogenisation temperature T_h (L+Vap → L) and of the vapour bubble radius $r(T)$ using a thermodynamic model that accounts for the effect of surface tension on liquid–vapour homogenisation.[17]

A second, low-density synthetic pure water inclusion (B) with ϱ = 826 kg/m^3 and a volume of about 2700 µm^3, was used to determine the temperature-dependent shift $(\partial \nu/\partial T)_{p=0}$ of the ice I_h Raman bands around 3100 cm^{-1} (O–H stretching mode) and at 220 cm^{-1} (lattice translational mode) along the water sublimation curve, i.e., virtually at zero pressure. Due to its low density inclusion B is in a

This journal is © The Royal Society of Chemistry 20xx

Please do not adjust margins

stable liquid–vapour two-phase state at room temperature, and consequently, the pressure follows along the saturation curve upon cooling until ice nucleation occurs (L+Vap → ice I_h +Vap). There, the pressure drops from saturation to sublimation pressure and the vapour bubble becomes slightly compressed due to the larger volume of ice I_h compared to liquid water. Ice melting (ice I_h +Vap → L+Vap) was observed at 0.0 °C, showing the characteristic feature of the triple point transition, namely the instantaneous melting of all the ice within 0.1 °C.

Experimental setup

Microthermometic measurements were performed using a Linkam THMS 600 heating/cooling stage mounted on an Olympus BX-41 upright microscope. The microscope was equipped with an Olympus LMPlanFL 100x/0.8 long-working distance objective for visual observation of the inclusions during microthermometric measurements. Temperature calibrations of the heating/cooling stage were performed using synthetic H_2O and H_2O-CO_2 fluid inclusion standards. The reference temperatures measured were the triple point of water (0.0 °C) and the triple point of CO_2 (–56.6 °C). The temperature accuracy of our measurements is estimated at ± 0.1 °C around 0 °C and at ± 0.2 °C below –40 °C, while precision (reproducibility) was ± 0.05 °C.

The microscope with the heating/cooling stage was attached to a T64000 triple spectrometer (Horiba) equipped with a back-illuminated, liquid nitrogen cooled CCD detector with 26 µm × 26 µm pixel size (SYMPHONY, Horiba). Calibration of the spectrometer was accomplished by means of the 521 cm^{-1} Raman peak of a silicon standard. In triple subtractive spectrometer configuration (three 1800 grooves/mm gratings) the setup allows the acquisition of Raman spectra in the low-frequency range as low as 10 cm^{-1}, though at the cost of signal intensity. For higher frequencies, a single spectrometer configuration was used (one 1800 grooves/mm grating and edge filter). A 514.5 nm argon-krypton laser (Coherent Innova 70 C) was used for Raman excitation. While the nominal output power of the laser is 300 mW, the effective laser power on the sample was about 20 mW and thus, low enough to avoid any measurable heating of the fluid inclusions, which was confirmed by the reproducibility of ice melting temperatures measured with and without laser irradiation of the sample. The spectral resolution of the system is 0.66 cm^{-1} at 220 cm^{-1} and 0.42 cm^{-1} at 3100 cm^{-1}.

Raman measurements were performed in back-scattering geometry using the Olympus LMPlanFL 100x/0.8 objective for focussing the laser beam into the sample and for collecting the Raman- and Rayleigh-scattered light. Furthermore, the setup was designed for polarisation-dependent Raman measurements featuring a rotatable half-wave plate in the excitation light path and a fixed, vertically oriented polariser in the light path of the back-scattered Raman signal.

Raman measurements

Raman spectroscopy was used in this study to identify different phases occurring during the microthermometric runs and to determine the pressure in the inclusion based on the shift of the ice I_h peak position.

Low-frequency Raman spectra were obtained in triple spectrometer configuration at temperatures between –0.4 and –80 °C. Using the 1800 grooves/mm gratings the spectral window ranges from 14 to 670 cm^{-1} and thus covers the lattice translational Raman bands of the different ice polymorphs. The spectra were obtained by averaging two measurements, each with 120 seconds acquisition time in order to reduce the signal-to-noise ratio. The crystallographic orientation of the quartz thick-section was set to extinction between crossed polarisers. Subsequently, Raman spectra were measured in xy (also denoted as HV) polarisation, where x (or H = horizontal) denotes the polarisation direction of the excitation laser and y (or V = vertical) the polarisation direction of the Raman signal measured in the spectrometer. Using this configuration, we were able to almost entirely suppress the strong A_1 Raman band of the quartz host occurring at about 206 cm^{-1} that superimposes the translational bands of ice I_h.

In addition to spectra of the ice phases in the inclusion we also measured the spectra of the quartz host next to the inclusion, at the same depth, the same temperatures and with the same acquisition time. Although the measurements were performed with a confocal setup using a 100 µm pinhole the intensities of the remaining quartz peaks were only little lower when the laser was focussed into the inclusion, which apparently is due the small volume of inclusion A, particularly, due to its small z-extension (about 3 µm) in axial direction of the laser focus. In comparison to this, the 20 times larger low-density inclusion B showed a dramatic decrease of the quartz signal, when focussing into the inclusion. Furthermore, the small volume of inclusion A made it impossible to measure a low-frequency Raman signal of supercooled liquid water, except for a characteristic broadening of the Rayleigh mode.

In contrast to the low-frequency measurements, Raman spectra of the O–H stretching bands were measured in single spectrometer configuration and yy (HH) polarisation using also a 1800 grooves/mm grating. Three spectral windows were necessary to cover the frequency range from 2710 to 3890 cm^{-1}. Acquisition time was 2 × 30 seconds for each window, indicating a significantly higher Raman intensity compared to the lattice translational bands. Hence, at high frequencies, we could also obtain the Raman spectrum of liquid water even of very small amounts.

A total of 276 individual Raman spectra were measured for this study.

Data treatment

The Raman raw spectra were corrected to account for shifts of the spectrometer using the reference peak position of the silicon standard measured at room temperature, as well as the position of the two low-frequency quartz bands at about 130 and 260 cm^{-1} at

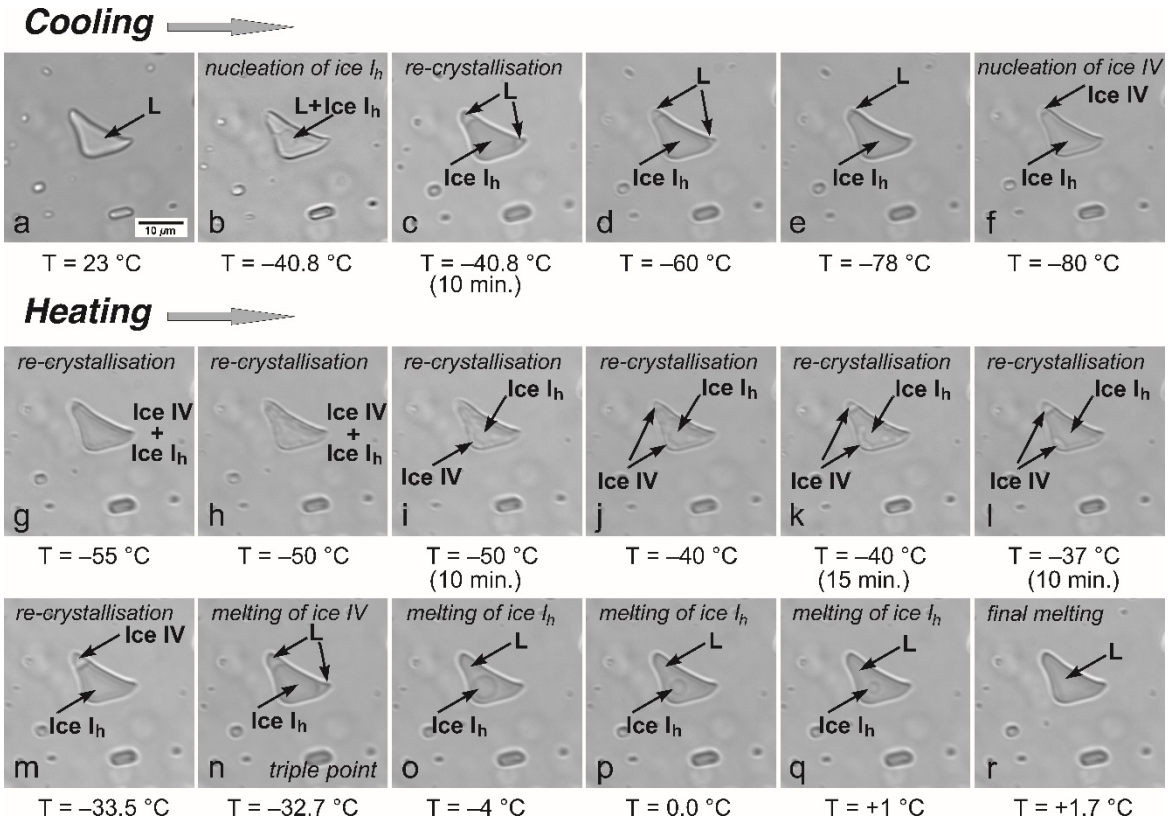


Figure 1: Series of photographs of inclusion A at different temperatures illustrating the phase transitions observed upon cooling and subsequent heating. A scale is indicated in image a. For a detailed description we refer to the text

known temperatures. The position of the dominant peak of the ice I_h O–H stretching band was determined directly from the spectrum with an estimated precision of about ± 1.5 cm^{-1}. The peak position of the lattice translational band of ice I_h was determined after subtraction of the normalised quartz spectrum taken at the same temperature. Here the uncertainty of the peak determination is estimated at ± 0.75 cm^{-1}.

Results

Microthermometric measurements

Figure 1 shows a sequence of photographs illustrating the phase changes observed in the high-density fluid inclusion A upon cooling (upper panel) and upon subsequent heating (lower panel). At 23 °C (Fig. 1a) the water in the inclusion is in a metastable liquid state at negative pressure, i.e., the liquid water is under tensile stress. Upon cooling the pressure in the inclusion further decreases, following a pseudo-isochoric trajectory (see Marti et al.[18]), reaches a pressure minimum, and finally increases again to positive pressure as illustrated in Fig 2.

On its re-entrant branch the liquid-isochore intersects the metastable extension of the saturation curve (L+Vap) at about –27 °C, which is referred to as retrograde liquid-vapour homogenisation temperature T_{hr} .[15,18] Upon further cooling, the nucleation of ice I_h (T_n I_h) was observed at about –41 °C (Fig 1b). Assuming that the nucleation temperature of ice I_h is close to the homogeneous nucleation limit T_H, the pressure at T_n I_h was calculated at 28 MPa using Equation A1 of Holten et al.[19] While ice nucleation takes place in the ice I_h stability field, the pressure in the inclusion increases abruptly upon freezing. Fig. 1c demonstrates that ice I_h does not entirely fill the inclusion volume but coexists with liquid water that has not completely transformed to solid. Thus, the phase transition occurring at T_n I_h is L ⟶ ice I_h + L. The presence of liquid water coexisting with ice I_h was confirmed by Raman spectroscopy (see Fig. 4b) and is corroborated by the convex shape of the ice I_h crystal boundary (Fig. 1c), which is characteristic for the liquid-solid interface. We note that the presence of liquid water promotes a rapid re-crystallisation of the initially polycrystalline ice to a single ice I_h crystal (*cf*. Fig. 1b and 1c).

Upon further cooling (Fig. 1d and 1e) ice I_h grows at the expense of the liquid phase, indicating a metastable equilibrium between the two phases. Reversely, ice I_h melts continuously upon heating following the image sequence e-c, n-q and in turn grows again upon cooling. At about –80 °C, finally, a phase transition occurs that results in an abrupt pressure drop (see Fig. 2). Although this phase transition could not be observed directly (Fig. 1f) we observed the re-crystallisation and coalescence of a second solid phase upon subsequent heating, starting at about –55 °C (Fig. 1g). We found strong evidence indicating that this newly formed phase is ice IV, a metastable, proton-disordered form of ice (*cf.* Fig. 4a and particularly Fig. 8a,b). Fig. 1g-m illustrate the sluggish re-

This journal is © The Royal Society of Chemistry 20xx

Please do not adjust margins

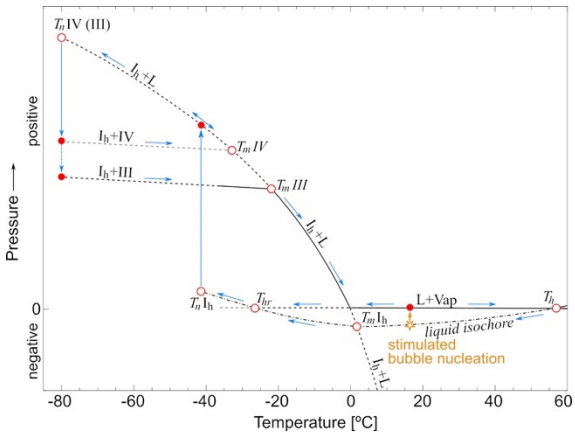


Figure 2: Schematic representation of the *p-T* trajectories (blue arrows) of inclusion A during the microthermometric runs. L+Vap: liquid-vapour equilibrium curve; I_h+L: ice I_h melting curve; I_h+IV: ice I_h-ice IV coexistence curve; I_h+III: ice I_h-ice III coexistence curve. Solid lines: stable phase states, dashed lines: metastable phase states. Below the liquid-vapour homogenisation temperature T_h the monophase liquid state of the inclusion becomes metastable (dash-dotted isochore), first with respect to vapour, then, below T_m I_h with respect to both vapour and ice I_h, and finally below T_{hr} with respect to ice I_h only. The orange star indicates the option to stimulate vapour bubble nucleation by means of ultra-short laser pulses,[16] which allowed us to measure T_h and T_{hr}, the temperatures of prograde and retrograde liquid-vapour homogenisation, respectively. T_n and T_m denote the nucleation, respectively the melting temperatures of the ice phases (I_h, III or IV). See text for further details.

crystallisation and coalescence process of ice IV that apparently formed from the liquid water film between the ice I_h crystal and the inclusion walls (ice I_h+L ⟶ ice I_h+ice IV). We assume that the re-crystallisation and coalescence of ice IV is likely caused by the Gibbs-Thomson effect, i.e., the depression of the equilibrium melting temperature as a function of the interfacial curvature of the ice crystals[20] that presumably are at the nanoscale when formed at –80 °C. The presence of an inter-crystalline liquid water film would promote re- crystallisation, resulting in an increase of the crystal grain size, and consequently, in an increase of the melting temperature. At about –34 °C (Fig. 1m) the two ice phases were completely separated featuring a nearly linear solid-solid interface between two single crystals, ice IV and ice I_h, respectively. In contrast to the ice I_h-liquid phase equilibria the volume ratio of ice IV and ice I_h does not perceivably change between –34 and –80 °C as illustrated in Fig. 3a.

At –32.7 °C (Fig. 1n), ice IV melts to liquid water (ice I_h+ice IV ⟶ ice I_h+L), defining a triple point that, to our knowledge, has not been described in the literature so far. After melting of ice IV, the remaining ice I_h, now coexisting with liquid water, melts continuously with increasing temperature (Fig. 1n-q) until final ice melting (T_m I_h) was observed at +1.7 °C (Fig. 1r), indicating that the inclusion has returned to the negative pressure domain.

The reproducibility of the ice IV nucleation temperature (T_n IV) is ± 1 °C, whereas the precision of the triple point and the final ice melting temperature is ±0.05 °C. Although our observations and microthermometric measurements have proven to be highly reproducible, there is still one exception: In one of the very last microthermetric runs we performed for this study, we observed that, after cooling the inclusion to –80 °C, ice III had formed instead of ice IV (ice I_h+L ⟶ ice I_h+ice III). Initially, we supposed that the formation of ice III was caused by the higher cooling rate we had used for this specific run (40 °/min). However, it turned out that the formation of ice III could not be reproduced reliably and formed, if at all, rather by chance. Upon subsequent heating ice III underwent a re-crystallisation and coalescence process similar to that observed with ice IV. After separation of the two coexisting ice phases, we found the volume of ice III to be significantly larger than that of ice IV. But, similar to the ice I_h-ice IV assemblage, the ice III/ice I_h volume ratio did not perceivably change between -24 and -80 °C (see Fig. 3b). The coexistence of ice III and ice I_h finally terminates at -22.0 °C (T_m III) in a triple point (ice I_h+ice III ⟶ ice I_h+L), which is in agreement with the respective triple point temperature reported by Bridgman.[3]

Raman spectra

Identification of phases. As mentioned above, the different phases occurring during the microthermometric runs were analysed by Raman spectroscopy and compared to reference spectra of different ice polymorphs reported by Minceva-Sukarova et al.[21] A compilation of Raman spectra of the different phases observed in this study is shown in Fig. 4a for the low-frequency lattice translational bands and in Fig. 4b for the high-frequency O–H

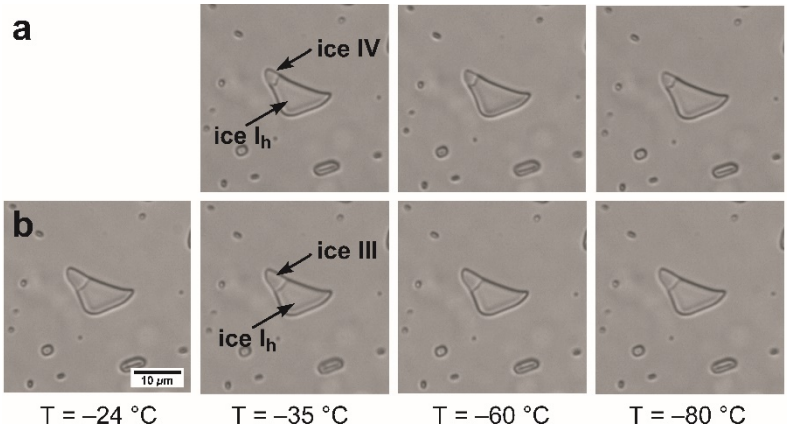


Fig. 3: Photographs illustrating **a)** the ice IV/ice I_h and **b)** the ice III/ ice I_h volume ratios. The volume ratios of the coexisting ice phases do not perceptibly change with temperature.

Please do not adjust margins

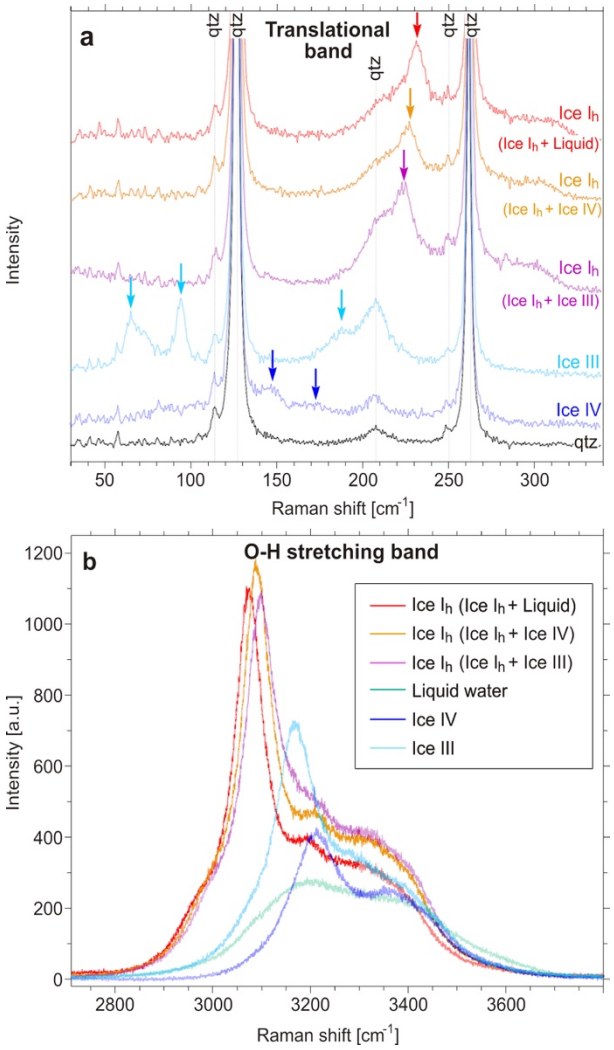


Figure 4: Raman spectra of ice I_h (red, orange and purple), ice III (light blue) and ice IV (blue) measured at -58.4 ºC. **a)** Low- frequency Raman spectra of the lattice translational bands. A quartz reference spectrum (black) measured in xy polariser configuration (see Section 2.3) is shown for comparison. **b)** High-frequency Raman spectra of the O–H stretching bands. The spectrum of liquid water coexisting with ice I_h is depicted in turquoise. The spectra of ice I_h represent three different phase assemblages with liquid water (red), with ice IV (orange) and with ice III (purple). The positions of the ice I_h peak reflect the different pressures at which the three phase assemblages coexist.

stretching bands. All spectra shown were taken at –58.4 °C including the quartz reference spectrum (black) in Fig. 4a.

Ice I_h could be clearly identified from the low-frequency spectrum with its characteristic peak at about 220 cm^{-1}. The spectra shown in Fig. 4 represent three different phase assemblages: ice I_h+L (red), ice I_h+ice IV (orange), and ice I_h+ice III (purple). The peak positions of ice I_h differ significantly, indicating that ice I_h is under different pressure depending on the phase assemblage.

The identification of ice IV (blue) was more difficult because of the low intensity of the translational bands in the Raman spectrum. The only ice IV reference spectra we could find in the literature are those reported by Salzmann et al.[22], which were recorded between -193 and -133 °C and at 1 bar pressure, and hence, at significantly different *p-T* conditions than our measurements (–58.4 °C, 281 MPa). Furthermore, their spectra were measured on polycrystalline samples, whereas in the present study, the spectra were taken from a single crystal of unknown crystallographic orientation. The low-frequency spectrum of ice IV shown in Fig. 4a exhibits a weak but clear band at about 150 cm^{-1} and a broad, rather vague band around 170 cm^{-1}. The two bands appear in all our ice IV spectra of the lattice translational mode and are clearly absent in the underlying quartz spectrum. For comparison, the low-frequency spectrum of Salzmann et al. recorded at –138 °C displays two major bands at about 150 and 175 cm^{-1} plus two minor bands at about 125 and 205 cm^{-1}. While the two major bands, conform quite well with those observed in our spectra, the latter two are not identifiable in our spectra because of the low signal intensity and the superposition with quartz bands. Our high-frequency spectrum of the O–H stretching bands, on the other hand, displays two broad peaks at about 3210 and 3350 cm^{-1}. The respective peak positions reported by Salzmann et al.[22] at –193 °C and 1 bar are at 3200 and 3330 cm^{-1}.

The identification of ice III (light blue) again appears quite clear, based on the distinct low-frequency Raman bands at about 65, 95, and 190 cm^{-1}, which are qualitatively in agreement with the corresponding spectrum reported by Minceva-Sukarova et al.[21] taken at –27 °C and 280 MPa. For comparison, the ice III spectra shown in Fig 4 were measured at –58.4 °C and 208 MPa. Although the spectra obtained in this study do not allow a clear discrimination between the proton-disordered ice III and ice IX, its proton-ordered equivalent, it is unlikely that the proton-ordered ice polymorph formed directly by nucleation from liquid water. We also note that the spectrum shown in Fig. 4a (lilac curve) exhibits a slightly higher intensity of the A_1 quartz band (206 cm^{-1}) compared to the other spectra. This is only partly due to the adjacent ice III band but mainly caused by a slight misalignment of the quartz orientation with respect to the Raman polarisation directions (xy configuration), which became obvious from the corresponding quartz reference spectrum (not shown in Fig 4a). The Raman spectrum of ice III in the O–H stretching region reported by Minceva-Sukarova et al.[21] (see their Fig. 5a) displays a sharp peak about 3150 cm^{-1} and a high, broad shoulder at about 3300 cm^{-1}. In our own high-frequency spectrum (Fig. 4b), however, the intensity of the 3300 cm^{-1} stretching band is very low and does not form a pronounced peak.

The identification of liquid water coexisting with ice I_h was possible only in the O–H stretching region (turquoise curve in Fig. 4b). At low frequencies, i.e., in triple spectrometer configuration, the signal intensity was too low and only the broadening of the Rayleigh band was observed.

Ice I_h peak positions. The broad Raman O–H stetching band of ice I_h is a superposition of 3 to 4 sub-bands with a dominant peak around 3100 cm^{-1} (e.g.[23,24]). The exact position of this peak depends on temperature and pressure, and shifts towards higher wave numbers with increasing temperature and towards lower wave numbers with increasing pressure. For the (low-frequency) lattice translational Raman band, in contrast, the shift of the peak position as a function

This journal is © The Royal Society of Chemistry 20xx

Please do not adjust margins

Table 1: Low- and high-frequency Raman peak positions of ice I_h measured for four different phase assemblages as a function of temperature

Temperature [°C]	Lattice translational band				O–H stretching band			
	Ice I_h peak pos. (I_h + L) [cm^{-1}]	Ice I_h peak pos. (I_h + IV) [cm^{-1}]	Ice I_h peak pos. (I_h + III) [cm^{-1}]	Ice I_h peak pos. (I_h + Vap.) [cm^{-1}]	Ice I_h peak pos. (I_h + L) [cm^{-1}]	Ice I_h peak pos. (I_h + IV) [cm^{-1}]	Ice I_h peak pos. (I_h + III) [cm^{-1}]	Ice I_h peak pos. (I_h + Vap.) [cm^{-1}]
-0.4	209.7			209.5	3154.7			3152.5 3152.0
-1.9	210.1				3148.1			3151.9
-5.8	213.6				3139.6			
-9.7	215.4 215.0			210.5	3132.2			3148.6 3148.8
-13.6	217.3				3126.1			
-17.5	218.7 219.0			211.7	3120.3			3145.3 3145.3
-19.4					3117.9 3117.6 3117.8			
-21.4	221.0				3114.4			
-24.3	221.6 221.7		221.1	212.7	3110.4 3111.0 3111.2		3112.4	3141.7 3142.5
-29.2	223.5 223.2				3104.6 3104.7 3104.5			
-32.7	224.6				3099.9			
-33.1	225.0	224.7 224.7		213.6	3100.0	3100.2		3138.8 3138.5
-36.0	225.3	225.0 225.0						
-37.9	226.0							
-38.9	226.3	225.5 225.4		213.7	3092.8	3097.8 3097.3 3097.1		3135.2 3136.3
-39.9					3091.9	3096.5		
-48.6	228.9 229.0	226.5 226.5		214.9	3083.9 3083.9	3094.0 3093.5		3132.0 3132.7
-58.4	231.6 231.7 231.6	227.1 227.0 227.3	224.2	215.3	3074.9 3075.5	3090.5 3090.2 3090.5 3090.6	3099.4	3128.8 3129.6
-68.1	233.3 233.6	227.8 227.8		216.2	3067.6	3087.0 3087.4		3126.7 3127.3
-77.9	235.3	228.5		216.9	3062.0	3082.6		3123.9 3124.0
-79.8		229.0				3082.4		

of *p* and *T* is exactly the opposite. The dominant ice I_h peak of the translational band is at around 220 cm^{-1}.

In the high-density inclusion A we observed ice I_h in three different phase assemblages: coexisting with liquid water (L), with ice IV, and with ice III. Additionally, ice I_h coexists with water vapour (Vap) in the low-density inclusion B. In Fig. 5 the measured ice I_h peak positions listed in Table 1 are plotted along these four coexistence lines as a function of temperature, both for the lattice translational band (a) and for the O–H stretching band (b). The colours of the data points indicate the different coexistence lines (red = ice I_h + L, orange = ice I_h + ice IV, purple = ice I_h + ice III, and blue = ice I_h + Vap). The Raman spectra of ice I_h were measured after complete re-crystallisation and separation of the coexisting ice phase (either ice IV or ice III). For the measurements along the sublimation curve inclusion B was heated to –0.1 °C to promote the re-crystallisation of ice I_h. Replicate measurements at specific temperatures were performed either at the end of a microthermometric cycle 2 – 4 hours after the initial measurement or several days later during a new temperature run. The reproducibility of the measurements was good and the data points describe a monotonic (non-linear) trend of the ice I_h peak position along the individual coexistence lines without any steps or distinctive kinks. Empirical fits of the data along the ice I_h melting and sublimation lines and along the ice I_h + ice IV coexistence line (Eq. (1)-(6)) are reported in Table 2. The data fits comply with a series of boundary conditions, 1. the ice I_h melting and the sublimation curve intersect at 0.01 °C, 2. the I_h melting curve and the ice I_h-ice IV coexistence curve intersect at –32.7 °C, 3. the deviation of the fit functions from the measured data

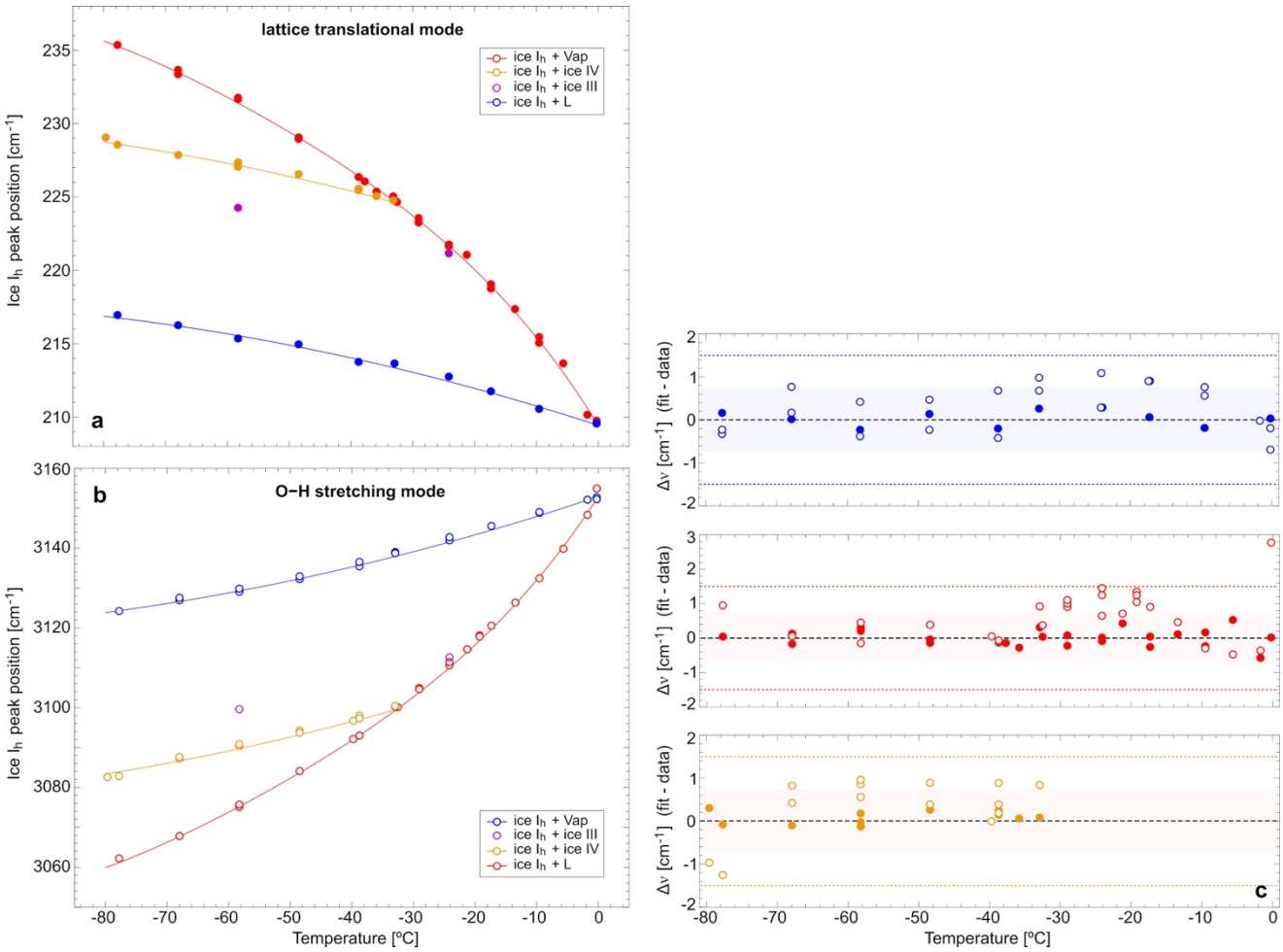


Figure 5: Measurements of ice I_h peak positions as a function of temperature (and pressure). **a)** lattice translational mode (filled circles) **b)** O–H stretching mode (open circles). Colors tag the four phases coexisting with ice I_h: liquid water (red), ice IV (orange), ice III (purple) and water vapour (Vap) (blue). Solid lines are fits to the measured data (see Eq. (1)-(6)). **c)** Deviation of the data from the corresponding fits. Except for one data point at -0.4 °C, all measurements are within the estimated precision (± 0.75 cm^{-1} for the lattice translational band (shaded area) and ± 1.5 cm^{-1} for the O–H stretching band (horizontal lines).

points is less than ± 1.5 cm^{-1} for the O–H stretching mode and less than ± 0.75 cm^{-1} for the lattice translational mode, and 4. the fits of the low- and of the high-frequency data eventually yield the same pressures for the ice I_h melting curve and the ice I_h-ice IV coexistence curve, respectively. The deviation of the individual data points from the fits are shown in Fig 5c with filled symbols representing the low-frequency data and open symbols for the high-frequency data. Except for a single high-frequency data point at –0.4 °C, the resulting deviations are smaller than the estimated uncertainties.

Table 2: Empirical fits to the ν-T data of ice I_h along the melting curve (ice I_h + L), the ice I_h-ice IV coexistence curve (ice I_h + ice IV) and the sublimation curve (ice I_h + Vap). Equations (1)-(3) refer to the lattice translational band and equations (4)-(6) to the O–H stretching band.

Binodal	**Ice I_h peak position: Lattice translational band**	Validity range [°C]	
ice I_h + L	ν [cm^{-1}] = 209.4476 – 6.826855·$10^{-1}T$ – 9.367985·$10^{-3}T^2$ – 9.510851·$10^{-5}T^3$ – 4.19475·$10^{-7}T^4$	0 to -80	(1)
ice I_h + ice IV	ν [cm^{-1}] = 220.3097 – 1.4932·$10^{-1}T$ – 5.483·$10^{-4}T^2$	-32.7 to -80	(2)
ice I_h + Vap	ν [cm^{-1}] = 209.44214 – 1.367092·$10^{-1}T$ – 5.476089·$10^{-4}T^2$	0 to -80	(3)
	Ice I_h peak position: O–H stretching band		
ice I_h + L	ν [cm^{-1}] = 3152.911 + 2.381942T + 3.202941·$10^{-2}T^2$ + 3.243083·$10^{-4}T3$ + 1.430337·$10^{-6}T^4$	0 to -80	(4)
ice I_h + ice IV	ν [cm^{-1}] = 3115.885 + 5.562891·$10^{-1}T$ + 1.95237·$10^{-3}T^2$	-32.7 to -80	(5)
ice I_h + Vap	ν [cm^{-1}] = 3152.92968 + 5.201679·$10^{-1}T$ + 1.9525139·$10^{-3}T^2$	0 to -80	(6)

This journal is © The Royal Society of Chemistry 20xx

Please do not adjust margins

For the ice I_h-ice III coexistence line we can report only four data points at -24.3 and -58.4 °C plus the triple point measurement at -22.0 °C. As previously mentioned, the appearance of ice III was observed for the first time at the very end of our Raman measurements and at the time we did not succeed to re-nucleate ice III after measuring the triple point temperature. Later on, we managed to produce ice III again by chance but using another microthermometric setup that was not coupled to a Raman spectrometer.

Temperature and pressure calibration of the ice I_h peak position. Numerical literature values of the temperature- and pressure-dependency of the ice I_h peak position, $(\partial \nu/\partial T)_{p = \text{const}}$ and $(\partial \nu/\partial p)_{T = \text{const.}}$, respectively, are sparse and in poor agreement.[21,25,26] For this reason, we re-calibrated the shift of the Raman peak position of ice I_h as a function of temperature and pressure for both, the O–H stretching and the lattice translational band. The results are shown in Table 3.

The temperature-dependent shift $(\partial \nu/\partial T)_{p = 0}$ was determined along the water sublimation curve using the low-density pure water inclusion B mentioned above. The data points (blue dots) shown in Fig 5 indicate a slightly non-linear trend of the ice I_h peak position. This non-linearity is in agreement with previous experimental data compiled by Shi et al.[27] (see their Fig. 7). The slope $(\partial \nu/\partial T)_{p = 0}$ of the ice I_h peak position is given by equation (7) for the lattice translational band and by equation (10) for the O–H stretching band.

The pressure-dependent shift of the ice I_h peak position, in contrast, could not be determined from direct measurements at constant temperature. Instead we used inclusion A to record the Raman peak positions $\nu_{p,T}$ along the ice I_h melting curve between 0 and –22 °C (see Fig. 5) and subtracted the temperature related ν_T portion of the shift using Eq. (7) and Eq. (10), respectively. The resulting $\Delta\nu$ value corresponds to the pressure-dependent portion ν_p of the Raman shift. Since $\Delta\nu = \nu_p = \nu_{p,T} - \nu_T$ we obtain positive ν_p values for the lattice translational mode and negative ν_p values for the O–H stretching mode. Using then the expression of Wagner et al.[28] for the *p*-*T* trend of the ice I_h melting curve (a polynomial fit to experimental data) we derived the pressure-dependent Raman shift $(\partial \nu/\partial p)_{T = \text{const}}$ of ice I_h for the lattice translational and for the O–H stretching mode. Although the slope $(\partial \nu/\partial p)_{T = \text{const}}$ was found to be nearly linear in the range between 0 and 208 MPa, we decided for a non-linear fit of the p-ν_p data, which eventually results in higher pressures when extrapolated beyond 208 MPa. The triple point pressure of 611.657 Pa at $\Delta\nu = 0$ was set as boundary condition for the data fit. The slopes of the resulting p-ν_p curves are given by equations (8) and (11) for the lattice translational band and for the O–H stretching band, respectively. The validity range of equations (8) and (11) is from 0 to 208 MPa but we shall extrapolate them up to 460 MPa. Since ν_p is the measured variable in our experiments we used equation (9) and (12) to calculate the ice pressure in the inclusions.

Table 3: Calibration of the temperature- and pressure-dependent shift of the Raman peak position of ice I_h for the lattice translational and the O–H stretching band. Note, the slopes $(\partial \nu/\partial T)_{p = 0}$ and $(\partial \nu/\partial p)_{T = \text{const}}$ are non-linear.

	Ice I_h peak position: Lattice translational band	Validity range	
p = const.	$(\partial \nu/\partial T)_{p = 0} = -0.13671 - 5.4761 \cdot 10^{-4} T$	0 to -80 ºC	(7)
T = const.	$(\partial \nu/\partial p)_{T = \text{const.}} = 0.0430 - 6.108 \cdot 10^{-6} \cdot p$	0 to 208 MPa	(8)
$p(\nu_p)$	$p = 6.2681 \cdot 10^{-4} + 23.1338 \cdot \nu_p + 9.295 \cdot 10^{-2} \cdot \nu_p^2$	0 to 208 MPa	(9)
	Ice I_h peak position: O–H stretching band		
p = const.	$(\partial \nu/\partial T)_{p = 0} = +0.520168 + 1.9525 \cdot 10^{-3} T$	0 to -80 ºC	(10)
T = const.	$(\partial \nu/\partial p)_{T = \text{const.}} = -0.1462 + 1.963 \cdot 10^{-5} \cdot p$	0 to 208 MPa	(11)
$p(\nu_p)$	$p = 6.1659 \cdot 10^{-4} - 6.78448 \cdot \nu_p + 7.99 \cdot 10^{-3} \cdot \nu_p^2$	0 to 208 MPa	(12)

The *p*-*T* phase diagram

Based on the fits of the ν-T data shown in Fig. 5 we finally calculated the *p*-*T* trend of the melting curve (ice I_h + L) between 0 and –80 °C and of the ice I_h-ice IV coexistences line between –32.7 and –80 °C, using the temperature and pressure calibrations of the ice I_h Raman shift described in the previous paragraph. Equations (13) and (14) reported in Table 4 describe the resulting *p*-*T* curves that are shown in the phase diagram in Fig. 6. In addition, the diagram displays the approximate trend of the ice I_h-ice III coexistence curve, based on the four data points obtained at –58.4 and –24.3 °C, and on the triple point temperature measured at –22.0 °C. Data points calculated from the measured low-frequency (filled circles) and high-frequency (open circles) peak position of ice I_h are shown in the respective colours. The deviation Δp of the individual data points from the calculated curves is shown in Fig. 7. The Δp-plots indicate a precision of the pressure determination of about ± 10 MPa for both the low- and the high-frequency data.

Figure 6 additionally displays the stability fields of liquid water, ice I_h, ice II (grey shaded area), ice III, and ice V (see ref. [3]) as a reference framework to contrast our results with. The respective solid-liquid and solid-solid binodals are shown

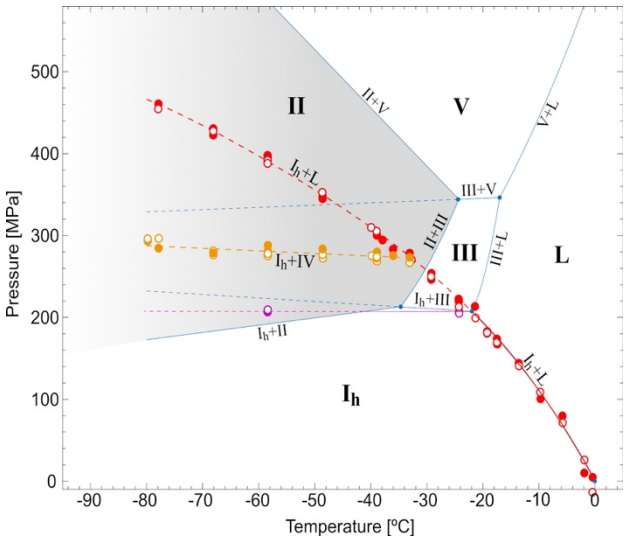


Figure 6: Detail of the *p-T* phase diagram of water showing the stability fields of liquid water (L), ice I_h, ice II, ice III and ice V and the respective phase boundaries (blue) based on experimental data from Bridgman[3]. Solid lines denote stable, dashed lines metastable phase equilibria. The ice I_h melting curve (red) and the ice I_h-ice IV coexistence curve (orange) were calculated from the fits of the measured ice I_h peak positions (Eq. (1)-(6)) using the pressure calibrations (Eq. (9) and Eq. (12)) described in Section 3.3. Filled circles denote data points derived from low-frequency, open circles from high-frequency Raman measurements. The approximate trend of the I_h-ice III equilibrium line (based on four data points) is shown in purple.

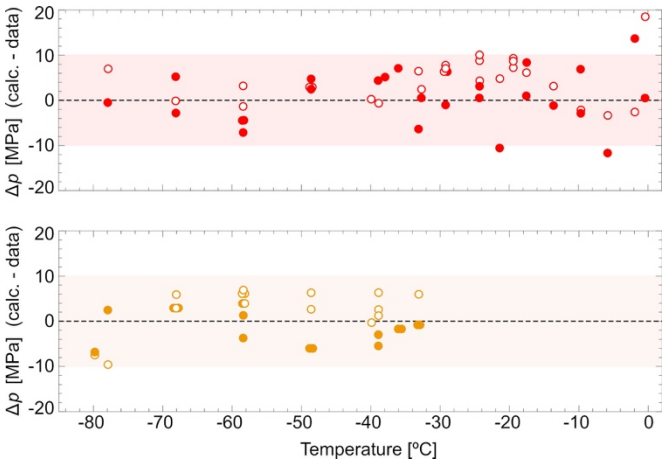


Figure 7: Deviation of the data points from the calculated ice I_h melting curve (red) and ice I_h-ice IV coexistence line (orange), respectively. The precision (not the accuracy) of the pressure derived from the Raman peak position of ice I_h is about ± 10 MPa, indicated by the shaded area. Filled circles represent data points derived from low-frequency Raman measurements, open circles those from high-frequency measurements.

in blue with solid lines for stable and dashed lines for metastable phase equilibria. Bridgman was probably the first who reported on the "prolongation of the I-L curve" below –22 °C (see ref. [3], p. 478). However, his ice I_h melting curve terminates at the ice I_h-ice III-liquid triple point. In the present study, we could trace the melting curve into the low-temperature metastable region down to –80 °C (red dashed line). Below –22.0 °C the two phases, ice I_h and liquid water, become metastable first, with respect to ice III and then, below –30 °C, with respect to ice II. At –80 °C and 466 MPa, the super-cooled ice I_h melting curve eventually terminates due to the nucleation of either ice IV or ice III. The nucleation of ice IV results in a pressure drop of approximately 180 MPa, while the pressure drop associated with the nucleation of ice III is about 260 MPa.

The ice I_h-ice IV coexistence curve calculated from the fits of the ν-*T* data exhibits a linear *p-T* trend with a slightly negative slope. Both phases are metastable with respect to ice II and their coexistence terminates at the intersection with the metastable ice I_h melting curve, forming a triple point of three metastable phases (ice I_h, ice IV and L) at –32.7 °C and 273 MPa.

The *p-T* trend of the ice I_h-ice III coexistence curve, finally, is not well constrained by our data. The two data points at –58.4 °C are located in the ice II stability field, and thus represent a metastable phase equilibrium, while the data points at –24.3 °C represent the stable phase equilibrium. The ice I_h-ice III-L triple point was measured at –22.0 °C and the pressure was determined at 207 MPa. While the triple point is in agreement with the measurements reported by Bridgman[3], we note that our data points at –58.4 °C plot clearly below Bridgman's ice I_h-ice III coexistence curve.

Table 4: Empirical equations describing the *p-T* trend of the ice I_h melting curve and the ice I_h-ice IV coexistence curve shown in Fig. 6.

Binodal	Equation: *p* [MPa], *T* [°C]	Validity range	
ice I_h+L	$p = 1.28108604 \cdot 10^{-1} - 12.74778 \cdot T - 1.915212 \cdot 10^{-1} \cdot T^2$ $- 2.01501 \cdot 10^{-3} \cdot T^3 - 8.775 \cdot 10^{-6} \cdot T^4$	0 to -80 °C	(13)
ice I_h+ice IV	$p = 262.294 - 0.316 \cdot T$	-32.7 to -80 °C	(14)

This journal is © The Royal Society of Chemistry 20xx

Please do not adjust margins

Discussion

Comparison with literature data. In order to draw a more complete picture of the metastable phase relations observed in this study and to compare our data, we have complemented the phase diagram with available data from the literature (Fig. 8a). Experimental data of the low-temperature metastable extension of the ice I_h melting curve have previously been measured by Mishima[8,29] using a water-emulsion technique. The scatter of these data (yellow dots) is somewhat larger than that of our data and the overall trend of Mishima's measurements indicates a slightly different curvature of the ice I_h melting line, leading to higher pressures in the metastable region and slightly lower pressures in the stable region above –22 °C. Considering experimental uncertainties of the two data sets, our results (red curve) are in acceptable agreement with Mishima's *p-T* data of the super-cooled ice I_h melting curve. In addition to the experimental data of Mishima, the diagram displays a calculated ice I_h melting curve derived by combination of the Equation of State (EoS) of ice I_h [30] and the EoS for super-cooled water [19]. This melting line (brown) again is slightly more curved in the metastable region but runs close to the minimum melting pressures determined by Mishima, and hence deviates only little from the melting curve obtained in this study. The third ice I_h melting curve shown in the diagram (dark grey), finally, was derived by extrapolation of the expression of Wagner et al.[28]. Below –22 °C this curve deviates progressively from the two other ice melting lines and eventually exceeds the maximum ice melting pressures measured by Mishima.

In order to explain the nucleation of either ice IV or ice III at –80 °C Fig. 8a displays experimental data (blue dots) of the homogeneous nucleation limit T_H.[9,31] The corresponding T_H curves were calculated using data fits of Holten et al.[19] (Eq. A1 and A2) that include additional experimental data in the range between 500 and 1500 MPa.[32] The homogeneous nucleation limit exhibits a break point at about –92 °C and 200 MPa. At low pressures the negatively sloped T_H curve is associated with the nucleation of ice I_h, whereas at high pressures the T_H curve has a positive slope and is associated with the nucleation of high-pressure ice polymorphs like ice III and ice IV. The intersection of the high-pressure branch of the T_H curve with our ice I_h melting curve (red) is at –78 °C. This is only two degrees higher than the nucleation temperature actually measured in this study. Our data, thus, suggest a slightly steeper slope of the T_H line. At this point we call the reader's attention to the fact that Mishima's data[8,29] indicate a continuation of the ice I_h melting curve at temperatures below the homogeneous nucleation limit. The reason is that Mishima observed in his experiments the compression-induced melting of ice I_h, starting with emulsified water droplets of 1-10 μm diameter, freezing them to ice I_h at low pressure and finally increasing pressure at constant temperature until the exothermic melting transition was recorded. Due to the small size of the droplets in the emulsion, the nucleation of secondary ice phases is kinetically suppressed, [32] which explains

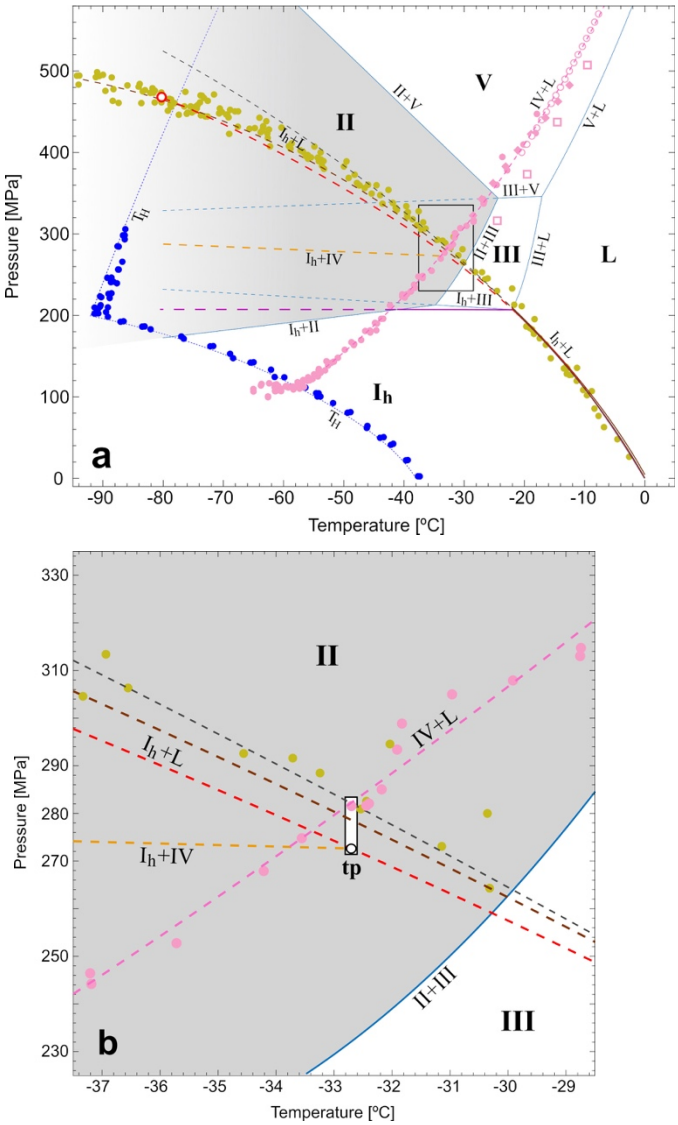


Figure 8: a) Detail of the *p-T* phase diagram of water like Fig. 6 but featuring additional experimental data from the literature: ice I_h melting pressures (yellow dots)[8,29], ice IV melting pressures represented by pink symbols (diamonds[4], open circles[33], open squares[6], dots[29]), and *p-T* data of the homogeneous nucleation limit T_H (blue)[9,31]. Three different representations of the ice I_h melting curve are shown based on: 1. the empirical expression of Wagner et al.[28] extrapolated below –22 °C (dark grey line), 2. the combination of the EoS for ice I_h[30] and the EoS for supercooled liquid water[19] (brown line) and 3. the peak positions of the ice I_h Raman bands (red; this study). The ice I_h-ice IV equilibrium curve is shown in orange. See text for further details. **b)** Enlarged detail of the marked area in a) illustrating the agreement of the ice IV melting curve with the ice I_h-ice IV-liquid triple point (tp) measured at –32.7 ±0.1 °C.

why the liquid produced by ice melting does not instantaneously freeze to a high-pressure ice phase. In case of the ice IV melting line, also shown in Fig. 8a, melting was induced by decompression of ice IV at constant temperature. And again, the melting curve seems to continue across the T_H curve. In this case, however, it is not a continuation of the ice IV melting curve, as indicated by the clear change of the slope close to T_H but, in fact, the data points below T_H are associated with an "ice IV-to-ice I_h transition" (*cf.* ref. [29]) that should not be confused with an ice IV-ice I_h equilibrium.

To our knowledge this is the first experimental study reporting on the existence of an ice I_h-ice IV coexistence line (orange) that terminates in a metastable triple point at the intersection with the ice I_h melting curve. To complete the picture Fig. 8a displays experimental data of the corresponding ice IV melting curve.[4,6,29,32,33] Since the measurements of Nishibata[6] (open squares) plot significantly below the other data points they were excluded from the data fit (pink dashed line). The resulting ice IV melting curve passes very close to the proposed triple point as illustrated in an enlarged view in Fig. 8b. At the triple point temperature of –32.7 ±0.1 °C the pressure of the fitted ice IV melting curve is about 10 MPa higher than the triple point pressure determined in this study. This pressure difference is within experimental uncertainties and we conclude that the three curves, in fact, intersect in the same *p*-*T* point. This finding confirms that the ice phase formed at –80 °C is in fact ice IV and that the ice I_h-ice IV coexistence curve is a thermodynamic, though metastable, equilibrium line.

Implications for fluid inclusion studies

Finally, we come back to the questions that initially motivated us to conduct the present study: Our results have clearly demonstrated that the ice phase present in the inclusion after nucleation is ice I_h even when pressure increases into ice II stability field. The low-temperature metastable extension of ice I_h-liquid binodal furthermore implies that the maximum pressure in the inclusion cannot exceed the melting curve. This in turn explains why irreversible volume changes do not increase with increasing bulk water densities of the inclusions. Preliminary microthermometric experiments using a synthetic fluid inclusion with a density ϱ of 995 kg/m^3, which is higher than that of inclusion A, shows larger L/ice I_h and ice IV/ ice I_h volume ratios, while T_n IV as well as the triple point temperature again were measured at –80 °C and –32.7 °C, respectively. This is a further proof that the pressure in the inclusion is controlled by metastable ice I_h-liquid and ice I_h-ice IV phase equilibria.

Our results also show that the quartz crystal hosting the fluid inclusions can withstand internal pressures of up to 466 MPa as well as abrupt pressure increases of 315 MPa upon nucleation of ice I_h without experiencing significant irreversible volume changes due plastic and/or brittle deformation. For inclusion A the resulting volume increase was found to be below 0.02 %, deduced from the increase of the liquid–vapour homogenisation temperature (T_h) from 56.8 °C (initial value) to 57.1 °C (measured after several freezing/melting cycles). However, we need to bear in mind that inclusion A was rather small (120 µm^3) and that the extent of overpressure an inclusion can withstand decreases with increasing size, which has been demonstrated by high-temperature decrepitation experiments (see Roedder[34], p. 70 ff).

Conclusions

The present study provides a wealth of new experimental data related to the low-temperature phase diagram of water. On the one hand, our results confirm, though with slight deviations, previous experimental data of Mishima[8,29] concerning the metastable extension of the ice I_h melting curve below the ice I_h-ice III-liquid triple point. On the other hand, our study revealed a new metastable equilibrium curve of ice I_h and ice IV that terminates in a triple point at –32.7 °C and 273 MPa. This triple point interlinks three metastable equilibrium curves: ice I_h + ice IV, ice I_h + liquid, and ice IV + liquid. With regard to the ice I_h-ice III equilibrium curve, however, further measurements are needed to confirm or disproof the apparent deviation from Bridgman's data.[3] And last but not least, the present study proposes a new, non-linear calibration of the temperature- and pressure-dependent shift of the ice I_h Raman bands for the lattice translational and for the O–H stretching mode. Although the present study has demonstrated that synthetic fluid inclusions can be applied for investigations of solid-liquid and solid-solid phase equilibria in the water phase diagram, further potential applications in this field are rather limited due to the isochoric nature of the experiments, in which the pressure is not an independent variable. A potential example for further applications would be the determination of pressure along the super-heated ice I_h melting curve. This, however, requires an extrapolation of the calibration curves of the ice I_h Raman shift to positive temperatures and negative pressures (tensile stress).

More than one century after Bridgman's pioneering work, our knowledge of the water/ice phase diagram, particularly with respect to metastable phase equilibria is still incomplete and the amount of available experimental data is moderate. New experimental studies are needed to confirm or improve the existing data, and potentially disclose new features of this enormously rich phase diagram of solid water.

List of symbols

p	pressure (MPa)
T	temperature (°C)
T_h	liquid-vapour homogenisation temperature
T_{hr}	retrograde liquid-vapour homogenisation temperature
T_H	(temperature of the) homogeneous nucleation limit
T_n	nucleation temperature of ice I_h, III or IV
T_m	melting temperature of ice I_h, III or IV
ν	Raman shift (cm^{-1})
ν_T	temperature-dependent Raman shift (cm^{-1}) at p = const.
ν_p	pressure-dependent Raman shift (cm^{-1}) at T = const.
ϱ	density (kg/m^3)

Conflicts of interest

There are no conflicts to declare

This journal is © The Royal Society of Chemistry 20xx

Please do not adjust margins

Acknowledgements

The authors thank Osamu Mishima for providing us with the numerical data of the ice I_h and ice IV melting curves. We also thank Max Wilke for producing the high-density fluid inclusion samples used in this study. This work has received support from the French Agency for Research (Agence Nationale de la Recherche, ANR) through the Equipex Planex ANR-11-EQPX-36 and the labex Voltaire ANR-10-LABX-100-01.

References

1 V.F. Petrenko and R.W. Whitworth, *Physics of ice*, Oxford University Press, 1999.
2 T. Bartels-Rausch, V. Bergeron, J.H.E. Cartwright, R. Escribano, J.L. Finney, H. Grothe, P.J. Gutiérrez, J. Haapala, W.F. Kuhs, J.B.C. Pettersson, S.D. Price, C.I. Sainz-Díaz, D.J. Stokes, G. Strazzulla, E.S. Thomson, H. Trinks and N. Uras-Aytemiz, *Rev. Mod. Phys.*, 2012, **84**, 885-944.
3 P.W. Bridgman, *Proc. Am. Acad. Arts and Sci.*, 1912, XLVII, **13**, 441-558
4 L.F. Evans, 1967. J. Appl. Phys., 1967, **38**, 4930-4932.
5 E. Roedder, *Science*, 1967, **155**, 1413-1417.
6 K. Nishibata, *Jpn. J. Appl. Phys.*, 1972, **11**, 1701-1708.
7 S.J. Henderson, and R.J. Speedy, *J. Phys. Chem.*, 1987, **91**, 3069-3072
8 O. Mishima, *Nature*, 1996, **384**, 556-559.
9 H. Kanno, R.J. Speedy, C.A. Angell, *Science*, 1975, **189**, 4206, 880-881.
10 O. Mishima, L.D. Calvert, E. Whalley, *Nature*, 1984, **310**, 393-395.
11 J.L. Green, D. J. Durben, G. H. Wolf, C. A. Angell, *Science*, 1990, **249**, 649-652.
12 Q. Zheng, D.J. Durben, G.H. Wolf, C.A. Angell, *Science*, 1991, **254**, 829-832.
13 K.I. Shmulovich, L. Mercury, R. Thiéry, C. Ramboz, M. El Mekki, *Geochim. Cosmochim. Acta*, 2009, **73**, 2457–2470.
14 M.E.M. Azouzi, C. Ramboz, J.-F. Lenain, F. Caupin, *Nat. Phys*., 2013, **9**, 38–41.
15 C. Qiu, Y. Krüger, M. Wilke, D. Marti, J. Rička, M. Frenz, *Phys. Chem. Chem. Phys.*, 2016, **18**, 28227-28241.
16 Y. Krüger, P. Stoller, J. Rička, M. Frenz, 2007. *Eur. J. Mineral*., 2007, **19**, 693-706.
17 D. Marti, Y. Krüger, D. Fleitmann, M. Frenz, J. Rička, *Fluid Phase Equilib*., 2012, **314**, 13-21.
18 D. Marti, Y. Krüger, M. Frenz, *ECROFI XX Abstracts*, 2009, 163-164
19 V. Holten, J.V. Sengers, M.A. Anisimov*, J. Phys.Chem. Ref. Data*, 2014, **43**, 1-23
20 W. Thomson, *Philos. Mag.*, 1871, **42**, 448.
21 B. Minceva-Sukarova, W.F. Sherman, G.R. Wilkinson, *J. Phys. C: Solid state Phys.*, 1984, **17**, 5833-5850.
22 C.G. Salzmann, I. Kohl, T. Loerting, E. Mayer, A. Hallbrucker, *J. Phys. Chem. B*, 2003, **107**, 2802-2807.
23 M.J. Taylor, E. Whalley, *J. Chem. Phys*.,1964, **40**, 1660-1664.
24 Q. Sun, H. Zheng, 2009. *Prog. Nat. Sci*., 2009, **19**, 1651–1654.
25 T.C. Sivakumar, H.A.M. Chew, G.P. Johari, 1978. *Nature*, 1978, **275**, 524-525.
26 G.E. Slark, A.K. Garg, W.F. Sherman, G.R. Wilkinson, *J. Mol. Struct.*, 1984, **115**, 161-164.
27 L. Shi, S.M. Gruenbaum, J.L. Skinner, *J. Phys. Chem. B*, 2012, **116**, 13821-13830.
28 W. Wagner, T. Riethmann, R. Feistel, A.H. Harvey, *J. Phys. Chem. Ref. Data*, 2011, **40**, 043103-1 - 043103-11.
29 O. Mishima, 2011. *J. Phys.Chem. B*, 2001, **115**, 14064-14067.
30 R. Feistel, W. Wagner, *J. Phys. Chem. Ref. Data*, 2006, **35**, 1021-1047.
31 H. Kanno, K. Miyata, *Chem. Phys. Lett.*, 2006, **422**, 507–512.
32 O. Mishima, H.E. Stanley, *Nature*, 1998, **392**, 164-168.
33 H. Engelhardt, E. Whalley, *J. Chem. Phys*., 1972, **56**, 6, 2678-2684.
34 E. Roedder, *Review in Mineralogy*, 1984, **12**, Mineralogical Society of America, Chelsea, Michigan.

Metastable phase equilibria in the ice II stability field. A Raman study of synthetic high-density water inclusions in quartz

A metastable ice I_h- ice IV equilibrium curve has been discovered in the ice II stability field and the corresponding metastable triple point (ice I_h-ice IV-liquid) was determined at –32.7 °C and 273 MPa.

